CHEMISTRY OF MATERIALS

Article

pubs.acs.org/cm

Phase Transitions, Chemical Expansion, and Deuteron Sites in the $BaZr_{0.7}Ce_{0.2}Y_{0.1}O_{3-\delta}$ Proton Conductor

Glenn C. Mather,*[,†] Gemma Heras-Juaristi,[†] Clemens Ritter,[‡] Rodolfo O. Fuentes,[§] Adilson L. Chinelatto,[∥] Domingo Pérez-Coll,[†] and Ulises Amador[⊥]

[†]Instituto de Cerámica y Vidrio, CSIC, Cantoblanco, 28049 Madrid, Spain

[‡]Institut Laue-Langevin, 71 Avenue des Martyrs, Grenoble 38042, France

[§]Departamento de Física de la Materia Condensada, CNEA, Av. Gral. Paz 1499, 1650 Buenos Aires, Argentina

[∥]Departamento de Engenharia de Materiais, Universidade Estadual de Ponta Grossa, Av. Gal. Carlos Cavalcanti, 4748, 84030-900-Ponta Grossa-PR, Brazil

[⊥]Departamento de Química, Facultad de Farmacia, Universidad CEU-San Pablo, Boadilla del Monte, 28668 Madrid, Spain

ABSTRACT: The crystal structure of the technologically relevant, high-temperature proton conductor $BaZr_{0.7}Ce_{0.2}Y_{0.1}O_{3-\delta}$ (BZCY72) has been studied by high-resolution neutron powder diffraction performed on a deuterated sample in the temperature range 10−1173 K, complemented with synchrotron X-ray diffraction in the range RT-1173 K. A volume discontinuity on heating indicates a first-order phase transition from orthorhombic (space group *Imma*) to rhombohedral symmetry ($R\bar{3}c$) between 85 and 150 K. A further transition to cubic symmetry ($Pm\bar{3}m$) takes place at ∼570 K, indicated to be second order from the temperature dependence of the octahedral tilt angle. The stability field of the cubic phase was extended on cooling in the dehydrated state to 85 K. Expansion/contraction of the unit-cell volume on heating in low vacuum and air, respectively observed by neutron diffraction and synchrotron X-ray diffraction, was described with a point-defect model involving the temperature dependence of the water content and thermal expansion. Isotropic strain in the hydrated state is apparent on analysis of the broadening of the neutron-diffraction reflections during heating and cooling cycles. Rietveld refinement of the low-temperature neutron data and Fourier nuclear-density maps were employed to locate the deuterium position at a distance of ∼0.90 Å from the bonding oxygen at 10 K.

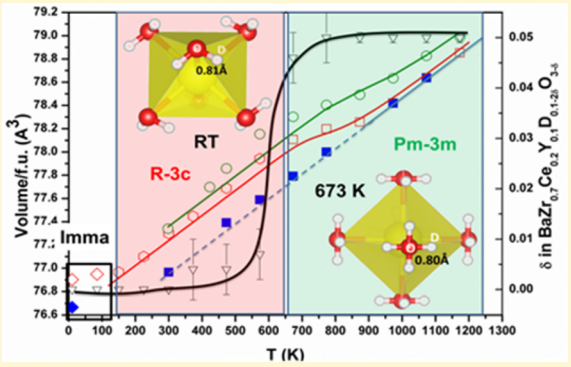

INTRODUCTION

High-temperature electrochemical devices exhibiting the preferential transfer of protons have the potential to revolutionize a shift to a sustainable energy economy in which hydrogen replaces dwindling hydrocarbon sources as the principal fuel for stationary power and transportation. Protonic ceramic fuel cells (PCFCs), with a proton-conducting ceramic electrolyte membrane, cleanly convert the chemical energy of hydrogen to electrical energy in an intermediate temperature range (773−1023 K).[1−3] This interval neatly alleviates the technological problems and costs associated with the higher operating temperatures of contemporary solid oxide fuel cells based on an oxide-ion conducting electrolyte and those of the polymeric devices which require expensive electrocatalysts due to the low operation temperature, below 373 K. Protonic ceramic electrolyzer cells (PCECs) also offer better performance in the intermediate temperature range 773−1023 K, and pure hydrogen is produced from steam, eschewing the need for costly purification steps prior to storage.[4−6] Membrane technologies based on proton-conducting ceramics for the reduction of CO_2,[7] separation of hydrogen from syn-gas,[8] and the nonoxidative conversion of natural gas to liquid fuel by the process of methane dehydroaromatization[9] are also garnering increasing attention.

The best proton-transport characteristics are observed in perovskite oxides (ABO_3) with large basic A cations (e.g., Ba, Sr) and large tetravalent B cations (e.g., Zr, Ce), which are doped with a lower valence cation on the B site to form oxygen vacancies in the dry state.[10,11] In water-containing atmospheres, the oxygen vacancies are replaced by hydroxyl groups with the second proton of the water molecule attaching to another lattice oxygen:

$$H_2O + V_o^{\cdot\cdot} + O_o^{\times} \rightarrow 2OH_o^{\cdot} \quad (1)$$

The materials of choice for PCFCs, hydrogen separators, and membrane reactors increasingly center on $Ba(Ce,Zr)O_{3-\delta}$-based solid solutions[7,12,13] for a compromise between moderately high proton conductivity and good stability, respectively offered by the $BaCeO_3$ and $BaZrO_3$ end-members. Much recent work

Received: March 17, 2016
Revised: June 6, 2016
Published: June 7, 2016

DOI: 10.1021/acs.chemmater.6b01095
Chem. Mater. 2016, 28, 4292−4299

adopts $BaZr_{0.7}Ce_{0.2}Y_{0.1}O_{3-\delta}$ (BZCY72, often referred to in the literature as BCZY27) as the optimized composition as development toward commercialization of proton-conducting membranes continues.[14−16] A full structural analysis is thus required for further understanding and development of this technologically important material.

In this regard, perovskites very often exhibit a number of symmetry changes with pressure, temperature, or composition associated with tilting of the BO_6 octahedra,[17−20] with the adopted tilt system very much guided by the tolerance factor.[21] Raman spectroscopy indicated a distortion of the "X-ray cubic" aristotype of BZCY72 to rhombohedral symmetry at room temperature.[13] This study highlights the advantage of complementing the determination of the crystal symmetry in these perovskites by methods additional to laboratory X-ray diffraction (XRD). The assignment of space group relies on the detection of supercell reflections attributable to subtle movements of the oxygen positions arising from octahedral tilting which are largely impercetible to X-rays due to the low X-ray scattering length of oxygen. In contrast, neutron diffraction is much more suited to determine symmetry changes as the neutron scattering length of oxygen is comparable with those of the cation species.

Here, we have employed high-resolution neutron diffraction, complemented by synchrotron radiation XRD data (SR-XRD), to perform a structural analysis of BZCY72 in the temperature range 10−1173 K, involving space-group determination and phase transitions with temperature, investigation of chemical expansion resulting from hydration, and location of deuteron sites. Deuterated samples were used in our study to avoid the large incoherent scattering cross-section of protons to thermal neutrons and improve the likelihood of locating deuterons within the oxide lattice. Neutron powder diffraction (NPD) data were collected at very low temperature (10 K) to freeze out the influence of phonon interactions and reduce thermal factors.

EXPERIMENTAL SECTION

$BaZr_{0.7}Ce_{0.2}Y_{0.1}O_{3-\delta}$ (BZCY72) was prepared by a citrate process based on the Pechini method. Prior to synthesis, the water content of the nitrate precursors was determined by thermogravimetry in air. The appropriate stoichiometric ratio of nitrates for 0.04 mol of product was added in the order $Ba(NO_3)_2{\cdot}xH_2O$, $ZrO(NO_3)_2{\cdot}xH_2O$, $Ce(NO_3)_3{\cdot}xH_2O$, and $Y(NO_3)_3{\cdot}xH_2O$ to deionized water heated at ∼323 K on a hot plate. Once a transparent solution was obtained, citric acid (0.2 mol) and ethylene glycol (0.4 mol) were added and stirred for ∼40 min. The temperature was then maintained in the range 333−353 K for ∼2 h then raised to >363 K for 4−5 h and finally to above 373 K for over 12 h to obtain a dark-brown polymerized complex. The material was subsequently pyrolyzed in an oven at 623 K for 4 h. The obtained polymeric precursor was then heated at 873 K for 4 h, milled, and heat treated at 1373 K for a further 4 h to remove any remaining organic product, prior to attrition milling in a Teflon vial with YSZ balls and sieving (100 μm). The powder was then formed into pellets, covered with sacrificial powder of the same composition, and fired at 1698 K for 4 h. The pellets were then crushed and milled in an agate mortar and pestle in acetone. Deuterated material for NPD was prepared on heating the as-prepared powder to 1173 at 5 K·min^{-1} in air bubbled through D_2O (Apollon Scientific, 99.9%) at room temperature (RT), followed by a 2 h dwell at this temperature then cooling to RT at 1 K·min^{-1}.

Phase purity was confirmed by powder XRD on a Bruker D8 high-resolution diffractometer, using monochromatic Cu Kα_1 radiation (λ = 1.5406 Å) obtained with a germanium monochromator. NPD measurements were performed on powders housed in vanadium cans at the high-resolution D2B diffractometer at the Institut Laue Langevin (Grenoble, France). Measurements of approximately 1 h in duration were collected at suitable intervals on heating and cooling cycles within a temperature range of 10−1073 K. Monochromatic beam wavelengths of 1.05 and 1.594 Å were selected from the primary beam with a Ge monochromator.

Synchrotron radiation X-ray diffraction (SR-XRD) was recorded at the D10B-XRD1 beamline at the National Synchrotron Light Laboratory (LNLS, Campinas, Brazil) on an as-prepared (undeuterated) sample mounted on a ceramic sample holder and heated in the range 298−1173 K. The X-ray wavelength was set at 1.54915 Å, and data were collected in the range $20 \le 2\Theta \le 90°$ with a step length of 0.005° and a step counting time of 2 s. The sample was heated at a rate of 10 K·min^{-1}, and a dwell time of 10 min was employed at each temperature before performing the SR-XRD scan. Structural refinements of the NPD and SR-XRD data were performed by the Rietveld method with the Fullprof program.[22]

RESULTS AND DISCUSSION

Structure of BZCY72 at RT. The neutron-diffraction pattern of BZCY72 obtained at 299 K (RT) revealed a distortion from the cubic perovskite aristotype, as indicated by the presence of several superlattice reflections, shown in Figure 1a. Employing the method of Woodward and Reaney,[23] based on the original arguments of Glazer,[24] the superstructure reflections could be

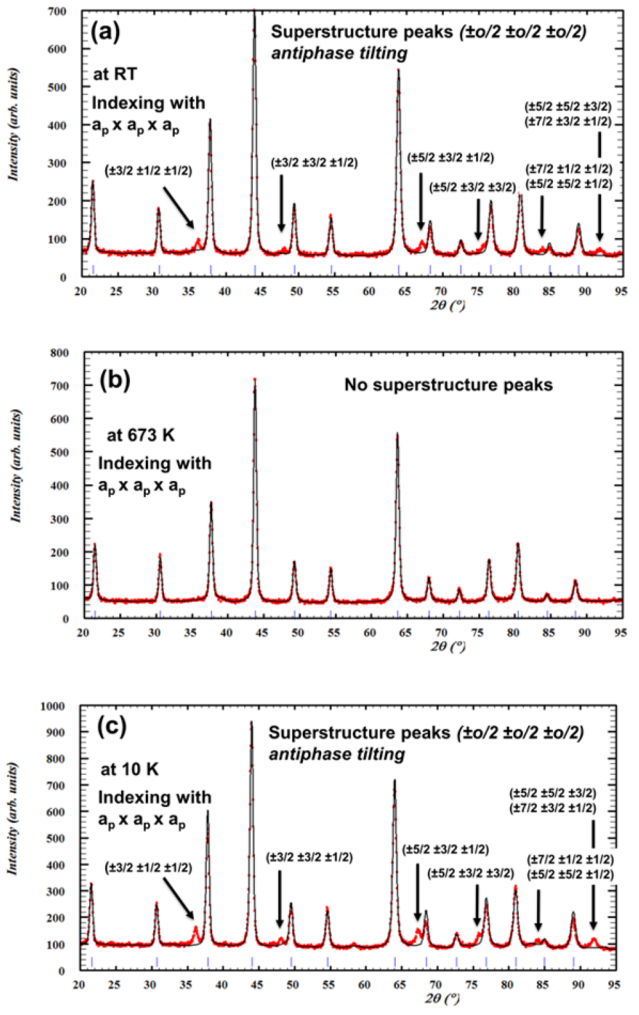

Figure 1. Experimental (circles) and calculated (continuous line) neutron diffraction patterns of BZCY72 collected on heating at (a) RT, (b) 673 K, and (c) 10 K, with an incident wavelength of 1.594 Å. The panels indicate superstructure reflections with a 1/2{*ooo*} indexation (where "*o*" indicates an index with an odd number) resulting from antiphase tilting.

DOI: 10.1021/acs.chemmater.6b01095
Chem. Mater. 2016, 28, 4292−4299

indexed as $^{1}/_{2}\{ooo\}$, where "o" represents an index with an odd number; this type of indexation is compatible with antiphase tilting only of the BO_6 octahedra. On consideration of the relationship between tilting system and space group, determined by Howard and Stokes through group-theoretical analysis,[25] the possible space groups were thus limited to $I4/mcm$, $Imma$, and $R\bar{3}c$. A transition to cubic symmetry around 573 K was immediately evident from the neutron-diffraction data (Figure 1b). The decrease in octahedral tilting in the transition toward cubic symmetry with increasing temperature was followed via the decreasing intensity of the reflection at 36°(2θ), which is indexed as (113) in a hexagonal cell (see below), Figure 2.

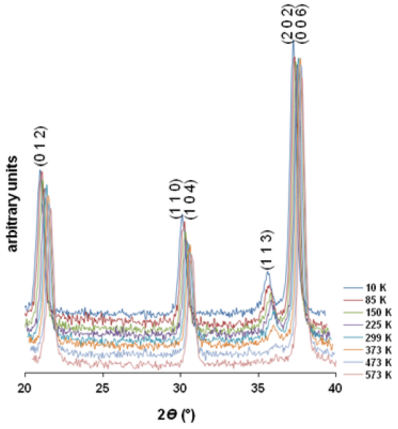

Figure 2. Selected region of the BZCY72 neutron diffraction pattern in perspective showing decreasing intensity of the (113) reflection of the $R\bar{3}c$ lattice (hexagonal coordinates) with increasing temperature, reflecting the transition to the $Pm\bar{3}m$ space group.

The continuous nature of this phase transition, discussed below, indicated that it was second-order in nature. Since the transition from $Imma$ to $Pm\bar{3}m$ is first order, the possible space groups for the RT structure based on the group−subgroup relationships of perovskites with octahedral tilting were further restricted to $I4/mcm$ and $R\bar{3}c$.[25] Refinements of the RT data were performed in these two space groups with the introduction of full oxygen occupancy in accordance with a completely hydrated material; anisotropic thermal factors improved the refinement quality criteria significantly. The final agreement parameters indicated that space group $R\bar{3}c$ was the more correct option in accord with the XRD and Raman spectroscopy analysis of Ricote et al.:[13] $\chi^2 = 1.66$, $R_{wp} = 4.92$, and $R_B = 3.20\%$ in $I4/mcm$ for 6 refined structure parameters (excluding profile parameters); $\chi^2 = 1.32$, $R_{wp} = 4.40$, and $R_B = 1.92\%$ in $R\bar{3}c$ for 7 refined parameters. The observed and calculated NPD patterns for BZCY72 at RT and their difference are shown in Figure 3a, with structural details listed in Table 1.

Structure Evolution with Temperature. The transformation to cubic symmetry, apparent in Figures 1b and 2, was followed with increasing temperature on calculation of the octahedral tilt angle (ϕ) from the refined oxygen position of the hexagonal cell.[26] The results, shown in Figure 4, indicate that the transition to cubic $Pm\bar{3}m$ symmetry appears to be complete by 573 K. The temperature dependence of ϕ (Figure 4) may provide information on the order of the phase transition.[27] The continuous nature of the transformation from 150 K on heating with a monotonic decrease of the tilt angle as the transition temperature (T_c) is approached indicates either a tricritical or second-order phase transition, rather than a first-order

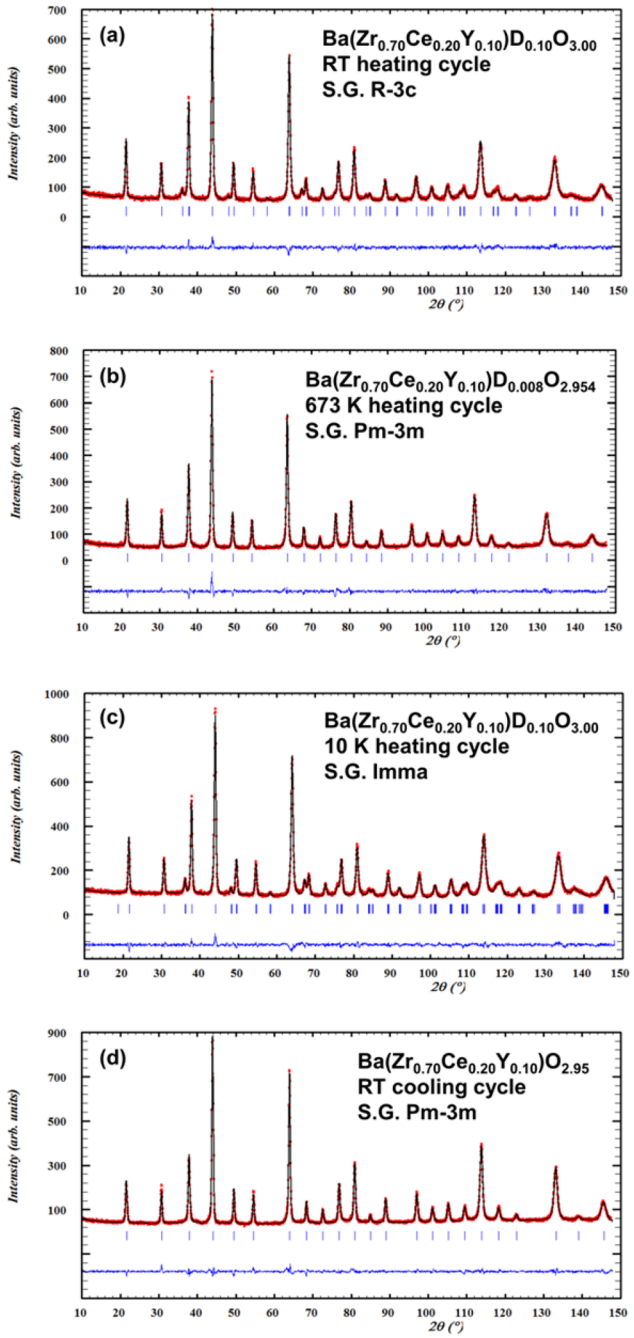

Figure 3. Experimental (circles), calculated (continuous line), and difference (continuous line at bottom of each panel) neutron diffraction patterns of BZCY72 collected on heating at (a) RT, (b) 673 K, (c) 10 K, and (d) RT on cooling; the incident wavelength is 1.594 Å, and the positions of Bragg peaks are indicated by vertical bars.

(discontinuous) transition in accordance with the group−subgroup relationship of $R\bar{3}c$ and $Pm\bar{3}m$.[25] The tricritical and second-order continuous transitions may be differentiated according to whether ϕ follows a $(T_c - T)^{\beta}$ temperature dependency with a β exponent of 0.25 or 0.5, respectively. In this case, it is apparent from the linear relationship between ϕ^2 and T (Figure 4) that the dependency of the tilt angle with temperature is a better fit with an exponent of $\beta = 0.5$ corresponding to a second-order phase transition (also plotted as ϕ on the secondary y axis of Figure 4). The behavior of BZCY72 through the $R\bar{3}c$-to-$Pm\bar{3}m$ transition contrasts with that of $BaPrO_3$, which

DOI: 10.1021/acs.chemmater.6b01095
Chem. Mater. 2016, 28, 4292−4299

Table 1. Structural Parameters, Selected Interatomic Distances, and Agreement Factors for BZCY72 Obtained from NPD Data at Three Representative Temperatures

	10 K (*Imma*)[a]	RT ($R\bar{3}c$)[b]	673 K ($Pm\bar{3}m$)[c]
a (Å)	6.0128(6)	6.0258(7)	4.2746(1)
b (Å)	8.490(1)	6.0258(7)	4.2746(1)
c (Å)	6.0210(6)	14.749(3)	4.2746(1)
V (Å^3)	307.36(9)	463.8(1)	78.107(4)
Ba position	4e	6a	1b
Z	0.000(2)	-	-
$U_{iso} \times 100$ (Å^2)	0.86(4)	0.70(8)	0.77(5)
Zr/Ce/Y position	4b	6b	1a
$U_{iso} \times 100$ (Å^2)	0.42(3)	0.20(8)	0.66(4)
O(1) position	4e	18e	3d
x	-	0.4760(2)	
z	0.5465(5)	.	-
Occ	1.00	1.00	0.9847(5)
$U_{iso} \times 100$ (Å^2)	0.33(4)	1.5(1)	1.6(3)
O(2) position	8g	-	3d
y	0.0123(4)	-	-
Occ	1.00	-	-
$U_{iso} \times 100$ (Å^2)	0.33(4)	-	-
D(1) position	8i	36f	12h
x	0.132(1)	0.151(4)	0.177(5)
y	-	0.388(6)	
z	0.604 (1)	0.0455(4)	-
Occ	0.025	0.017	0.00067(5)
$U_{iso} \times 100$ (Å^2)	0.14(6)	1.7(6)	0.9(1)
D(2) position	16j	-	-
x	0.106(1)	.	-
y	0.009(1)	.	-
z	0.191(1)	.	-
Occ	0.0125	.	
$U_{iso} \times 100$ (Å^2)	0.14(6)	.	
selected distances (Å)			
Ba–O(1)	3.020(4) × 2	3.158(1) × 3	3.023(1) × 12
	2.730(8)	2.868(1) × 3	
	3.290(8)	3.0149(5) × 6	
Ba–O(2)	3.079(9) × 4	-	
	2.933(9) × 4	-	
Zr/Ce/Y–O(1)	2.1408(8) × 2	2.1348(6) × 6	2.1373(1) × 6
Zr/Ce/Y–O(2)	2.1298(8) × 4		
O(1)–D(1)	0.86(3)	0.81(6)	0.76(7)
O(2)–D(2)	0.94(4)		

[a]Space group *Imma*, (No. 74): 4b (0 0 1/2), 4e (0 1/4 *z*), 8g (1/4 *y* 1/4), 8i (*x* 1/4 *z*),16j (*x y z*). χ^2 = 1.47, R_{exp} = 3.11%, R_{wp}= 3.77%, R_B = 1.97%, $\rho_{(cryst)}$: 6.184(2) g/cm^3. [b]Space group $R\bar{3}c$, hexagonal setting (No. 62): 6a (0 0 1/4), 6b (0 0 0), 18e (*x* 0 1/4), 36 f (*x y z*). χ^2 = 1.26, R_{exp} = 3.82%, R_{wp}= 4.30%, R_B = 1.74%, $\rho_{(cryst)}$: 6.147(8) g/cm^3. [c]Space group $Pm\bar{3}m$ (No. 221): 1a (0 0 0), 1b (1/2 1/2 1/2), 3d (1/2 0 0), 12h (*x* 1/2 0). χ^2= 2.42, R_{exp} = 4.09%, R_{wp}= 6.37%, R_B = 3.50%, $\rho_{(cryst)}$: 6.084(5) g/cm^3.

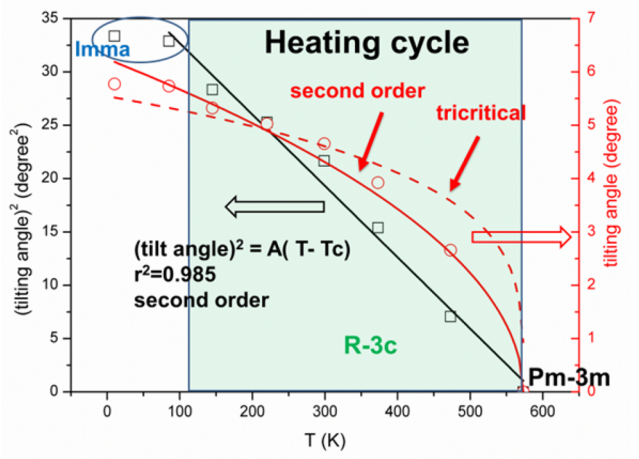

Figure 4. Square of the octahedral tilt angle (ϕ) as a function of temperature, (squares, primary *y*-axis), and ϕ as a function of temperature (circles, secondary *y*-axis) fitted with the power laws $\phi = \left(1 - \frac{T}{T_c}\right)^{0.25}$ (dashed red line) and $\phi = \left(1 - \frac{T}{T_c}\right)^{0.5}$ (solid red line) representing tricritical and second-order phase transitions, respectively.

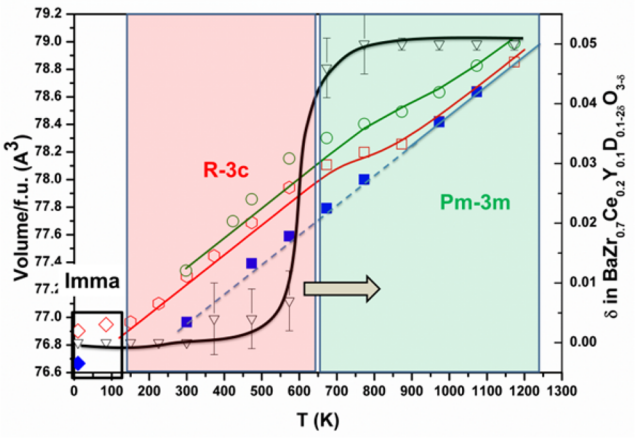

Figure 5. Experimental (symbols) and calculated (colored lines) pseudocubic lattice constant of BZCY72 determined from neutron diffraction data on heating (open red symbols) and cooling (blue closed symbols) in low vacuum and synchrotron X-ray diffraction data (open green symbols) on heating in air. The calculated data employs a model based on thermal expansion and chemical expansion due to hydration; pH_2O values of 1×10^{-3} and 2×10^{-2} atm were adopted for NPD and SR-XRD experiments, respectively. The oxygen loss occurring from the nominal formula of the hydrated material on heating as determined from refinement of the oxygen occupancy of the NPD data is also shown with reference to the secondary *y*-axis (inverted black triangles, with black line shown as guide for the eye). The crystallographic fields indicated in the plot refer to the space groups determined from the NPD data during the heating cycle in low vacuum.

is reported as tricritical.[28] It can be seen that the 10 K data point is not accurately described by the relation $\phi = \left(1 - \frac{T}{T_c}\right)^{0.5}$, reflective of a discontinuous phase transition taking place between 85 and 150 K, discussed below. The fitting of the experimental NPD pattern to that calculated using the structural model given in Table 1 for BZCY72 at 673 K is shown in Figure 3b.

Inspection of the pseudocubic lattice parameters and cell volume from 10 to 1173 K, Figure 5, reveals a discontinuity below 150 K. This transition is thus likely to be first-order in nature according to Landau theory, and, consequently, with no group–subgroup relationship between the space groups.[25] On the basis of the similar indexation of the 10 K data (Figure 1c) with that of the RT structure, a transition from either an *I*4/*mcm* or *Imma* structure at 10 K to $R\bar{3}c$ above 85 K seems to occur. The latter phase transformation, *Imma* to $R\bar{3}c$, has previously been observed in $BaCeO_3$ and $BaZrO_3$-based systems,[17,29,30] as well as $BaPrO_3$.[28] Although the more common sequence is from *Imma*

DOI: 10.1021/acs.chemmater.6b01095
Chem. Mater. 2016, 28, 4292–4299

to $I4/mcm$ to $Pm\bar{3}m$, stabilization of the intermediary rhombohedral phase has been associated with larger B cations.[28] Improved refinement quality criteria in *Imma* compared to either $R\bar{3}c$ or $I4/mcm$ space groups confirmed that the orthorhombic symmetry is the correct choice for the BZCY72 sample at both 10 and 85 K. The observed and calculated NPD patterns and their difference for BZCY72 at 10 K are shown in Figure 3c, with structural details listed in Table 1.

Location of Deuteron Sites. Fourier nuclear-density maps were calculated for the 10 K data with incident neutron wavelengths of both 1.04 and 1.594 Å in order to locate missing nuclear-scattering density arising from the deuterons, as has been performed for a number of oxide proton conductors.[31,32] Inspection of the density maps at both acquired resolutions, such as those illustrated in Figure 6, revealed strong positive

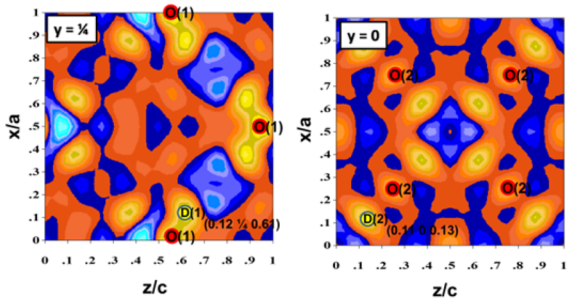

Figure 6. Fourier-difference nuclear maps in the *ac* plane calculated for the structure at 10 K in space group *Imma*, at heights of $y = 0.25$ (left panel) and $y = 0$ (right panel), showing missing scattering density attributable to D.

peaks, consistent with the positive scattering length of deuterium (6.671 fm), at (~0.12, ~1/4, ~0.61) and (~0.11, ~0, ~0.13) at a reasonable distance of ~1 Å from oxygen, corresponding to Wyckoff positions 8i and 16j in space group *Imma*, respectively. Refinement proceeded with inclusion of deuteron at these two positions close to the O(1) and O(2) sites, which refined stably with an occupancy slightly higher than that expected for full hydration, suggesting full occupancy of the oxygen substructure as a result of complete hydration. The final refinement was thus performed with a fixed D occupancy of 0.1, giving considerably improved agreement parameters in comparison to the deuteron-free refinement, e.g., R_B decreased by 26% (from 2.66% to 1.97%). The low-temperature deuteron position also refined stably on transformation to the higher symmetry $R\bar{3}c$ and $Pm\bar{3}m$ space groups with increasing temperature. The final structural parameters and agreement factors for BZCY72 collected at 10, 299, and 473 K are listed in Table 1 with inclusion of the D position. The final O−D distance, in the range 0.76−0.94(6) Å, is in line with values determined in similar systems both by diffraction methods (0.93 Å for $BaCe_{0.9}Y_{0.1}O_{3-\delta}$,[33] 0.92 Å for $BaZr_{0.5}In_{0.5}O_{3-\delta}$,[34] 1.06 Å for $BaCe_{0.4}Zr_{0.4}Sc_{0.2}O_{3-\delta}$[31]), atomistic-simulation techniques (0.98 Å for $BaZrO_3$[35]), and quantum-mechanical studies (0.89−1.05 Å for $BaCeO_3$[36]). The rather short distances determined at higher temperatures may be due to large thermal factors and lower deuteron occupancy, both of which lead to more uncertainty in the atomic positions.

Schematic diagrams of the location of the deuteron site relative to a BO_6 octahedron in the *Imma*, $R\bar{3}c$, and $Pm\bar{3}m$ structures are shown in Figure 7.

At low temperature (orthorhombic symmetry, 10−85 K) there are two independent deuteron sites: the O−B−O−D(1) torsion

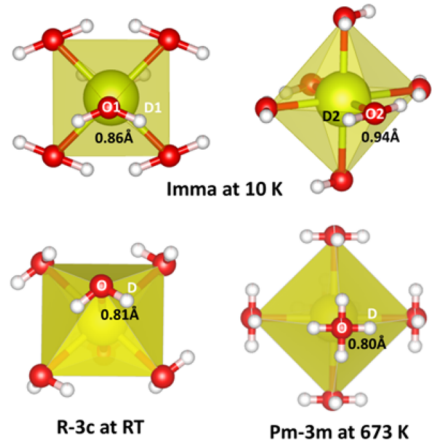

Figure 7. Schematic diagrams of the D position (white spheres) in relation to oxygen (red spheres) and the BO_6 octahedra (yellow) for three temperatures with different symmetries. Note that the statistical site occupancy of the D position is 0.1.

angle is 22° with the O−D(1) bond forming an angle of 51° with the O−O bond defining the octahedron edge, a location that is close to that of the "ring-like" rotational path between octahedral units suggested by quantum molecular dynamics.[37] This position minimizes the Coulombic repulsion of the neighboring B and Ba^{2+} cations, since the former are at a distance of 2.35 Å whereas the shortest Ba^{2+} to deuteron separation is 2.31 Å. A similar site near the O−O octahedron edge has been found for $BaZr_{0.5}In_{0.5}O_{3-\delta}$,[34] BCY20[32] (both by neutron diffraction), and $SrZrO_3$[38] (by muon-spin relaxation spectroscopy). The second deuteron D(2) lies closer to an octahedral edge, with the nearest B cation found at a shorter distance of 1.97 Å; however, the Ba^{2+} ions are located further away at 2.43 Å, which may compensate the effect of the shorter B−D(2) distance. This position appears to be more similar to that reported for $BaCe_{0.8}Y_{0.2}O_{2.9}$ (BCY20),[32] in which only one site was reported in *Imma* symmetry at 450 °C.

At higher temperature (RT), in the rhombohedral domain, only one deuteron position exists, the O−D bonds forming angles of 51° and 37° with the octahedral edges. The shortest D−B and D−Ba^{2+} distances are 2.15 and 2.41 Å, respectively. In cubic symmetry the sole deuteron lies parallel to the plane bisecting the octahedron forming an angle of 45° with the octahedron edge at a distance of 2.68 Å from the B cations and a shorter distance of 2.54 Å from the Ba ions (structure at 673 K).

Chemical and Thermal Expansion. In addition to revealing the discontinuous nature of the low-temperature phase transition of BZCY72 on heating from 10 K under low vacuum, Figure 5 also shows the corresponding pseudocubic lattice parameter data during cooling from 1173 K, together with data collected by SR-XRD on heating an as-prepared sample in air from RT. The Vegard's plots exhibit a nonlinear inconsistency on heating which can be attributed to a contraction resulting from dehydration. The loss of water can also be followed via the refined oxygen occupancy with temperature (secondary axis) in accordance with eq 1. Such behavior has previously been observed for Y-doped $BaZrO_3$ and $BaCeO_3$ proton-conducting phases.[39,40] The temperature of inflection to the contracted cell, ~673 K, occurs after the transformation to cubic symmetry. On cooling in the dehydrated state, the Vegard's plot is linear to RT, with a thermal expansion of 3.82×10^{-5} Å·K^{-1}. The value is slightly higher for the hydrated material, 4.49×10^{-5} Å·K^{-1}, in

DOI: 10.1021/acs.chemmater.6b01095
Chem. Mater. 2016, 28, 4292−4299

the range RT−573 K on heating. A similar trend was observed for $BaCe_{0.8}Y_{0.2}O_{2.9}$, with a higher TEC registered in the hydrated state than for the dry material,[40] although the opposite trend was found in the same work for $BaZrO_3$-based phases.

Although the phase transition to cubic symmetry on heating is not coincident with the dehydration temperature, the state of hydration has a clear effect on symmetry, as indicated by the stability to lower temperature of the cubic phase field on cooling in the dehydrated state (Figure 5, blue squares); the observed and difference diffraction profiles of the cubic $Pm\bar{3}m$ structure on cooling to RT are shown in Figure 3d. Again, similar behavior was observed for BCY20 on heating in air and cooling in low vacuum;[40] however, the BCY phase goes through a more complex series of transitions on heating and cooling through orthorhombic and monoclinic symmetries. It was argued in this case that structural relaxation around dopant−vacancy pairs is responsible for destabilizing the correlated octahedral tilts of the higher symmetry phase, leading to a greater stability field for the cubic structure in dry conditions.[32]

Previously, it was widely believed that the formation of positively charged oxygen vacancies via oxygen loss in oxide lattices led to electrostatic repulsion of the surrounding cations contributing to cell expansion; however, recent computer simulation indicates that chemical expansion only results from radius expansion of the reduced cation, whereas the formation of an oxygen vacancy leads to an opposite contracting effect.[41] In the case of proton-conducting oxides, which lose water to form oxygen vacancies (eq 1) with no change in cation valence states, the overall effect of dehydration is to produce the volume contraction observed in Figure 5. A further consequence of dehydration is a slight increase of the Goldschmidt tolerance factor from 0.984 (hydrated state) to 0.985 (dehydrated state); for calculation of the tolerance factor ionic radii were adopted from Shannon[42] considering an oxygen vacancy radius of 1.18 Å and OH^- radius of 1.35 Å.[40] Although this difference is very minor, it is salient to note that the two states lie at either side of a boundary marking antiphase tilting and cubic phase fields defined by a large number of perovskites at 0.985.[43] The stability of the cubic phase field of BZCY72 to lower temperatures in the dry state may, thus, be attributable not only to the effect of destabilization of the correlated octahedral tilts but partly owing to geometry expressed by the fact that the Goldschmidt tolerance factor is displaced to a higher value when the oxygen vacancies are not occupied by hydroxyl groups.

As discussed by Andersson et al.,[40] such an expansion on hydration produces significant compressional stress on the surface of the proton-conducting membrane as the oxygen vacancies nearer to the surface are hydrated, whereas a tensional stress occurs on dehydration at the surface, which is an important element contributing to mechanical failure. Here, the effect of stress is clearly observed through analysis of the full width at half maxima (fwhm) of the neutron-diffraction peaks during hydration and dehydration cycles, shown for the (400) reflection of the cubic subcell in Figure 8.

The fwhm lowers continuously on heating before reaching a fairly steady value above the dehydration temperature (~973 K);

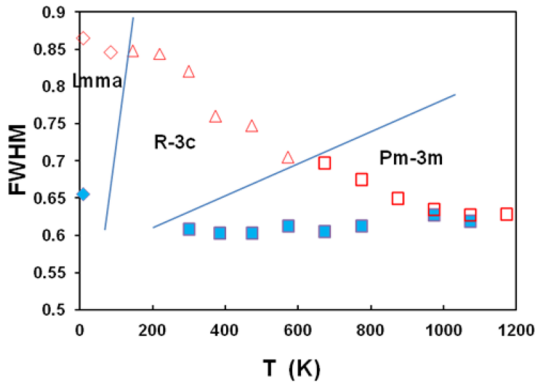

Figure 8. Full width half-maximum of the (400) reflection of the basic cubic cell during heating (red open symbols) and cooling (blue closed symbols) of a hydrated BZCY72 sample under low vacuum.

the fwhm then remains at a consistent lower value on cooling of the dehydrated sample in the dry conditions. We note that the peakwidth was broadened for all reflections in the hydrated state, with no evidence of a directional preference for strain, reflecting isotropic expansion of the lattice on incorporation of water molecules (eq 1). Andersson et al.[40] make the case that an inhomogeneous water distribution due to slow hydration kinetics may contribute to strain-induced line broadening of the diffraction profiles. Alternatively, even if the grains are fully hydrated, it may be that there are effects of disorder brought about by an inhomogeneous distribution of the octahedral tilting, and indeed this be related to the presence of water.

Modeling of the effects of dehydration on the crystal structure was performed based on a simple defect-chemistry model to describe the unit-cell volume in terms of temperature and water content.[40] Assuming ideal behavior for all species involved in the hydration equilibrium (eq 1), the equilibrium constant may be expressed as

$$K_{H_2O} = \frac{[OH_o^{\cdot}]^2}{[V_o^{\cdot\cdot}][O_o^{\times}]p_{H_2O}} = \exp\left(-\frac{\Delta H_M}{RT} + \frac{\Delta S_M}{R}\right) \quad (2)$$

The molar enthalpy and entropy, ΔH_M and ΔS_M, were taken as -137.95 kJ mol^{-1} and -144.2 J (mol·K)$^{-1}$ on assuming that the Zr:Ce ratio imposes a linear variation in the thermodynamic parameters between the corresponding thermodynamic values of the end-member $BaZr_{0.9}Y_{0.1}O_{3-\delta}$ and $BaCe_{0.9}Y_{0.1}O_{3-\delta}$ phases, taken from ref 11.

On assuming the site balance

$$[O_o^{\times}] + [V_o^{\cdot\cdot}] + [OH_o^{\cdot}] = 3 \quad (3)$$

and that the dopant concentration $x = Y_B'$ is distributed solely on the B site such that the electroneutrality condition is

$$2[V_o^{\cdot\cdot}] + [OH_o^{\cdot}] - x = 0 \quad (4)$$

the water content is then given by

$$[OH_o^{\cdot}] = \frac{3Kp_{H_2O} - \sqrt{Kp_{H_2O}(9Kp_{H_2O} - x[6Kp_{H_2O} - 24] + x^2[Kp_{H_2O} - 4])}}{Kp_{H_2O} - 4} \quad (5)$$

DOI: 10.1021/acs.chemmater.6b01095
Chem. Mater. 2016, 28, 4292−4299

The effect of hydration on volume expansion was analyzed following the approach of Marrocchelli et al.[41] and modified for the case of proton-conducting oxides by Andersson et al.[40] The lattice parameter of the cubic perovskite is approximated as

$$a = 2(\overline{r}_B + \overline{r}_O) \quad (6)$$

where

$$\overline{r}_O = \frac{1}{3}\left[\left(3 - \frac{x}{2} - \frac{y}{2}\right)r_{O_o^x} + \left(\frac{x}{2} - \frac{y}{2}\right)r_{V_o^{\cdot\cdot}} + y r_{OH_o^{\cdot}}\right] \quad (7)$$

with $\overline{r}_O$ and $\overline{r}_B$ representing the average oxide-ion and cation-site radii, respectively, and $y = [OH^{\bullet}]$. Ionic radii were adopted from Shannon,[42] with an oxygen vacancy radius $r_{V_o^{\cdot\cdot}}$ of 1.18 Å and hydroxyl group radius $r_{OH_o^{\cdot}}$ of 1.35 Å[40] once again employed. Thermal expansion was modeled with the relation

$$a_{o,T} = a_{o,300} + \alpha T \quad (8)$$

where a value of $\alpha \sim 4 \times 10^{-5}$ Å·K^{-1}was adopted corresponding to that measured in the dehydrated state in the range 973−1173 K. The model was then adjusted with a normalization factor of $\frac{a_{300,expt}}{a_{300,calc}} = 0.989$ where numerator and denominator correspond to experimental and calculated pseudocubic lattice parameters at 300 K. A good fit of the model to the data was achieved on applying the normalization factor and a water-vapor partial pressure of $p_{H_2O} = 1\times 10^{-3}$ atm for the diffraction environment, Figure 5; this value is reasonable considering the degassing process which takes place on heating within the vanadium container during the NPD experiment.

For comparison, also plotted in Figure 5 is the corresponding model of the experimental data collected in laboratory air by SR-XRD for a BZCY72 sample previously cooled at 5 K·min^{-1} (also in laboratory air). The effect of the higher water vapor partial pressure in this experiment, taken as $p_{H_2O} = 2 \times 10^{-2}$ atm, is to increase slightly the temperature at which dehydration occurs, as is expected, and the contraction is less pronounced than in the case of the sample measured at lower p_{H_2O}. We note that, irrespective of the thermal history of the sample, the model predicts complete hydration in both cases below the dehydration temperature. The good fit of the modeled data thus indicates a high level of hydration of the BZCY72 samples despite their different thermal histories.

CONCLUSIONS

The $BaZr_{0.7}Ce_{0.2}Y_{0.1}O_{3-\delta}$ (BZCY72) perovskite is emerging as one of the strongest candidates for a number of applications involving high-temperature proton transport, including protonic ceramic fuel cells, protonic ceramic electrolyzer cells, and reactor membranes for processes such as methane dehydroaromatization. A detailed analysis by high resolution neutron diffraction and synchrotron X-ray diffraction highlights several structural complexities of this technologically important phase. As is the case for similar proton-conducting perovskites, the phase stability is highly dependent on the degree of hydration. A transition from orthorhombic to rhombohedral symmetry occurs above 85 K on heating and then from rhombohedral to cubic symmetry at ∼570 K for the hydrated material (diffracting medium, low vacuum), but the latter transition occurs below RT on cooling in the dehydrated state. The hydrated condition, which is preserved above the phase-transition temperature, is associated with chemical cell expansion and strain broadening of the neutron-diffraction peaks, with cell contraction and alleviation of strain taking place on heating to dehydration.

The two deuteron sites of a deuterated sample at 10 K (space group, *Imma*) are similar to those of chemically similar perovskites, lying close to a plane bisecting the O−O octahedral edge at a distance of ∼0.90 Å from the bonding oxygen and ∼2 Å from the neighboring B-cation sites.

AUTHOR INFORMATION

Corresponding Author

*(G.C.M.) E-mail: mather@icv.csic.es.

Notes

The authors declare no competing financial interest.

ACKNOWLEDGMENTS

This work was supported by the MINECO, Spain (ENE2012-30929 and MAT2013-46452-C4-1-R), CSIC, Spain (i-link0743), and CAPES, Brazil (PVE, Proceso 88881.03418/2013-1). Access to the neutron facilities at the Institut Laue Langevin (Grenoble, France) and the National Synchrotron Light Laboratory (Campinas, Brazil) under Grant 5-24-55(D2B) and research proposal D10B-XRD1-16166, respectively, is gratefully acknowledged. U.A. also thanks CAM (S2013/MIT-2753) and the Universidad CEU San Pablo for financial support.

REFERENCES

(1) Coors, W. G. Protonic Ceramic Fuel Cells for High-Efficiency Operation with Methane. *J. Power Sources* **2003**, *118* (1−2), 150−156.

(2) Fabbri, E.; Pergolesi, D.; Traversa, E. Materials Challenges toward Proton-Conducting Oxide Fuel Cells: A Critical Review. *Chem. Soc. Rev.* **2010**, *39* (11), 4355−4369.

(3) Iwahara, H. Prospect of Hydrogen Technology Using Proton-Conducting Ceramics. *Solid State Ionics* **2004**, *168* (3−4), 299−310.

(4) Iwahara, H.; Esaka, T.; Uchida, H.; Maeda, N. Proton Conduction in Sintered Oxides and Its Application to Steam Electrolysis for Hydrogen Production. *Solid State Ionics* **1981**, *3*−*4*, 359−363.

(5) Stuart, P. A.; Unno, T.; Kilner, J. A.; Skinner, S. J. Solid Oxide Proton Conducting Steam Electrolysers. *Solid State Ionics* **2008**, *179* (21−26), 1120−1124.

(6) Sakai, T.; Matsushita, S.; Matsumoto, H.; Okada, S.; Hashimoto, S.; Ishihara, T. Intermediate Temperature Steam Electrolysis Using Strontium Zirconate-Based Protonic Conductors. *Int. J. Hydrogen Energy* **2009**, *34* (1), 56−63.

(7) Xie, K.; Zhang, Y.; Meng, G.; Irvine, J. T. S. Electrochemical Reduction of CO_2 in a Proton Conducting Solid Oxide Electrolyser. *J. Mater. Chem.* **2011**, *21* (1), 195.

(8) Matsumoto, H.; Okada, S.; Hashimoto, S.; Sasaki, K.; Yamamoto, R.; Enoki, M.; Ishihara, T. Hydrogen Separation from Syngas Using High-Temperature Proton Conductors. *Ionics* **2007**, *13* (2), 93−99.

(9) Rosensteel, W. A.; Sullivan, N. P. Fabrication of a Novel $BaCe_{0.8}Y_{0.2}O_{3-\delta}$ - Cu Ceramic-Metallic Composite Membrane for Hydrogen Separation. *ECS Meeting Abstracts*; 2015; pp MA2015−01 1511.

(10) Norby, T. Solid-State Protonic Conductors: Principles, Properties, Progress and Prospects. *Solid State Ionics* **1999**, *125* (1-4), 1−11.

(11) Kreuer, K. D. Proton -Conducting Oxides. *Annu. Rev. Mater. Res.* **2003**, *33* (1), 333−359.

(12) Ricote, S.; Bonanos, N.; Manerbino, A.; Coors, W. G. Conductivity Study of Dense $BaCe_xZr_{(0.9-x)}Y_{0.1}O_{(3-\delta)}$ Prepared by Solid State Reactive Sintering at 1500 °C. *Int. J. Hydrogen Energy* **2012**, *37* (9), 7954−7961.

(13) Ricote, S.; Bonanos, N.; Marco de Lucas, M. C.; Caboche, G. Structural and Conductivity Study of the Proton Conductor $BaCe_{(0.9-x)}Zr_xY_{0.1}O_{(3-\delta)}$ at Intermediate Temperatures. *J. Power Sources* **2009**, *193* (1), 189−193.

DOI: 10.1021/acs.chemmater.6b01095
Chem. Mater. 2016, 28, 4292−4299

(14) Robinson, S.; Manerbino, A.; Grover Coors, W.; Sullivan, N. P. Fabrication and Performance of Tubular, Electrode-Supported $BaCe_{0.2}Zr_{0.7}Y_{0.1}O_{3-\delta}$ Fuel Cells. *Fuel Cells* **2013**, *13* (4), 584−591.
(15) Vasileiou, E.; Kyriakou, V.; Garagounis, I.; Vourros, a.; Stoukides, M. Ammonia Synthesis at Atmospheric Pressure in a Ba-$Ce_{0.2}Zr_{0.7}Y_{0.1}O_{2.9}$ Solid Electrolyte Cell. *Solid State Ionics* **2015**, *275*, 110−116.
(16) Rørvik, P. M.; Haavik, C.; Griesche, D.; Schneller, T.; Lenrick, F.; Wallenberg, L. R. Chemical Solution Deposition of Thin Films for Protonic Ceramic Fuel Cells. *Solid State Ionics* **2014**, *262*, 852−855.
(17) Knight, K. S. S. Structural Phase Transitions, Oxygen Vacancy Ordering and Protonation in Doped $BaCeO_3$: Results from Time-of-Flight Neutron Powder Diffraction Investigations. *Solid State Ionics* **2001**, *145* (1−4), 275−294.
(18) Howard, C. J.; Knight, K. S.; Kennedy, B. J.; Kisi, E. H. The Structural Phase Transitions in Strontium Zirconate Revisited. *J. Phys.: Condens. Matter* **2000**, *12*, L677−L683.
(19) Gómez-Pérez, A.; Pérez-Flores, J. C.; Ritter, C.; Boulahya, K.; Castro, G. R.; García-Alvarado, F.; Amador, U. Structure Evolution with Sr Content of the Perovskite-like Materials $La_{2-x}Sr_xCoTiO_6$ ($0 \leq X \leq 0.5$). *J. Appl. Crystallogr.* **2014**, *47* (2), 745−754.
(20) Antunes, I.; Mather, G. C.; Frade, J. R.; Gracio, J.; Fagg, D. P. Stability of $Ba(Zr,Pr,Y)O_{3-\delta}$ Materials for Potential Application in Electrochemical Devices. *J. Solid State Chem.* **2010**, *183* (12), 2826−2834.
(21) Colla, E. L.; Reaney, I. M.; Setter, N. Effect of Structural Changes in Complex Perovskites on the Temperature Coefficient of the Relative Permittivity. *J. Appl. Phys.* **1993**, *74* (5), 3414−3425.
(22) Rodriguez-Carvajal, J. Recent Advances in Magnetic Structure Determination by Neutron Powder Diffraction. *Phys. B* **1993**, *192*, 55−69.
(23) Woodward, D. I.; Reaney, I. M. Electron Diffraction of Tilted Perovskites. *Acta Crystallogr., Sect. B: Struct. Sci.* **2005**, *61*, 387−399.
(24) Glazer, A. M. Simple Ways of Determining Perovskite Structures. *Acta Crystallogr., Sect. A: Cryst. Phys., Diffr., Theor. Gen. Crystallogr.* **1975**, *31* (6), 756−762.
(25) Howard, C. J.; Stokes, H. T. Group-Theoretical Analysis of Octahedral Tilting in Perovskites. *Acta Crystallogr., Sect. B: Struct. Sci.* **1998**, *54*, 782−789.
(26) Howard, C. J.; Kennedy, B. J.; Chakoumakos, B. C. Neutron Powder Diffraction Study of Rhombohedral Rare-Earth Aluminates and the Rhombohedral to Cubic Phase Transition. *J. Phys.: Condens. Matter* **2000**, *12* (4), 349−365.
(27) Glerup, M.; Knight, K. S.; Poulsen, F. W. High Temperature Structural Phase Transitions in $SrSnO_3$ Perovskite. *Mater. Res. Bull.* **2005**, *40* (3), 507−520.
(28) Knee, C. S.; Magrasó, A.; Norby, T.; Smith, R. I. Structural Transitions and Conductivity of $BaPrO_3$ and $BaPr_{0.9}Y_{0.1}O_{3-\delta}$. *J. Mater. Chem.* **2009**, *19* (20), 3238.
(29) Pagnier, T.; Charrier-Cougoulic, I.; Ritter, C.; Lucazeau, G. A Neutron Diffraction Study of $BaCe_x Zr_{1-X}O_3$. *Eur. Phys. J.: Appl. Phys.* **2000**, *9* (1), 1−9.
(30) Genet, F.; Loridant, S.; Ritter, C.; Lucazeau, G. Phase Transitions in $BaCeO_3$: Neutron Diffraction and Raman Studies. *J. Phys. Chem. Solids* **1999**, *60*, 2009−2021.
(31) Azad, A. K.; Irvine, J. T. S. Location of Deuterium Positions in the Proton-Conducting Perovskite $BaCe_{0.4}Zr_{0.4}Sc_{0.2}O_{2.90}{\cdot}xH_2O$ by Neutron Powder Diffraction. *Chem. Mater.* **2009**, *21*, 215−222.
(32) Eriksson Andersson, A. K.; Selbach, S. M.; Grande, T.; Knee, C. S. Thermal Evolution of the Crystal Structure of Proton Conducting $BaCe_{0.8}Y_{0.2}O_{3-\delta}$ from High-Resolution Neutron Diffraction in Dry and Humid Atmosphere. *Dalt. Trans.* **2015**, *44*, 10834−10846.
(33) Knight, K. Powder Neutron Diffraction Studies of Ba-$Ce_{0.9}Y_{0.1}O_{2.95}$ and $BaCeO_3$ at 4.2 K: A Possible Structural Site for the Proton. *Solid State Ionics* **2000**, *127* (1−2), 43−48.
(34) Ahmed, I.; Knee, C. S.; Karlsson, M.; Eriksson, S. G.; Henry, P. F.; Matic, A.; Engberg, D.; Börjesson, L. Location of Deuteron Sites in the Proton Conducting Perovskite $BaZr_{0.50}In_{0.50}O_{3-Y}$. *J. Alloys Compd.* **2008**, *450* (1−2), 103−110.
(35) Stokes, S. J.; Islam, M. S. Defect Chemistry and Proton-Dopant Association in $BaZrO_3$ and $BaPrO_3$. *J. Mater. Chem.* **2010**, *20* (30), 6258−6264.
(36) Münch, W.; Seifert, G.; Kreuer, K.; Maier, J. A Quantum Molecular Dynamics Study of Proton Conduction Phenomena in $BaCeO_3$. *Solid State Ionics* **1996**, *88*, 647−652.
(37) Münch, W.; Seifert, G.; Kreuer, K. D.; Maier, J. A Quantum Molecular Dynamics Study of the Cubic Phase of $BaTiO_3$ and $BaZrO_3$. *Solid State Ionics* **1997**, *97*, 39−44.
(38) Hempelmann, R.; Soetratmo, M.; Hartmann, O.; Wappling, R. Muon Diffusion and Trapping in Proton Conducting Oxides. *Solid State Ionics* **1998**, *107*, 269−280.
(39) Hiraiwa, C.; Han, D.; Kuramitsu, A.; Kuwabara, A.; Takeuchi, H.; Majima, M.; Uda, T. Chemical Expansion and Change in Lattice Constant of Y-Doped $BaZrO_3$ by Hydration/Dehydration Reaction and Final Heat-Treating Temperature. *J. Am. Ceram. Soc.* **2013**, *96* (3), 879−884.
(40) Andersson, A. K. E.; Selbach, S. M.; Knee, C. S.; Grande, T. Chemical Expansion Due to Hydration of Proton-Conducting Perovskite Oxide Ceramics. *J. Am. Ceram. Soc.* **2014**, *97*, 2654−2661.
(41) Marrocchelli, D.; Bishop, S. R.; Tuller, H. L.; Yildiz, B. Understanding Chemical Expansion in Non-Stoichiometric Oxides: Ceria and Zirconia Case Studies. *Adv. Funct. Mater.* **2012**, *22*, 1958−1965.
(42) Shannon, R. D. Revised Effective Ionic Radii and Systematic Studies of Interatomic Distances in Halides and Chalcogenides. *Acta Crystallogr., Sect. A: Cryst. Phys., Diffr., Theor. Gen. Crystallogr.* **1976**, *32* (5), 751−767.
(43) Reaney, I. M.; Colla, E. L.; Setter, N. Dielectric and Structural Charcterisation of Ba- and Sr-Based Complex Pervoskites as a Function of the Tolerance Factor. *Jpn. J. Appl. Phys.* **1994**, *33*, 3984−3990.

DOI: 10.1021/acs.chemmater.6b01095
Chem. Mater. 2016, 28, 4292−4299